Photoinduced transition to charge-ordered phases from dynamical localization in the metallic phase of α-(BEDT-TTF)_{2}I_{3}

Koudai Oya and Akira Takahashi

Phys. Rev. B **97**, 115147 — Published 23 March 2018

DOI: 10.1103/PhysRevB.97.115147

Photoinduced transition to charge-ordered phases from dynamical localization in the metallic phase of α-(BEDT-TTF)$_2$I$_3$

Koudai Oya[1] and Akira Takahashi[1,2*]

[1] *Graduate School of Engineering, Nagoya Institute of Technology, Gokiso-Cho, Showa-ku, Nagoya 466-8555, Japan and*

[2] *CREST, Japan Science and Technology Agency, Chiyoda-ku, Tokyo 102-0075, Japan*

(Dated: March 9, 2018)

Abstract

From theory, we investigate charge localization induced by higher-frequency off-resonance light-pulse excitation in the metallic phase of α-(BEDT-TTF)$_2$I$_3$ by numerically solving the time-dependent Schrödinger equation in the quarter-filled extended Hubbard model for the material. Around $eaA^{(\max)} = 1$, where $eaA^{(\max)}$ is the maximum amplitude of the dimensionless vector potential of the pump pulse, the charge distribution is significantly changed by photoexcitation, and the light-pulse-induced collective charge oscillations continue after photoexcitation. Furthermore, the charge dynamics depend strongly on the polarization direction of the pump pulse. These results are consistent with experiment. The magnitudes of the effective transfer integrals are reduced by strong photoexcitation, and this precursory phenomenon for dynamical localization is mainly driven by a photoinduced change in the ratio of the effective transfer integrals between the two strongest bonds. For $eaA^{(\max)} \gtrsim 2$, the photoinduced transition to the charge-ordered state, which can be regarded as a light-dressed state, occurs because of dynamical localization. Furthermore, the type of photo-generated charge-ordered state can be controlled by choosing $eaA^{(\max)}$ and the polarization direction.

I. INTRODUCTION

Photoinduced phase transitions[1–5] have been observed in various materials, and it is expected that the investigation of the phenomena will lead to ultrafast control of material phases and discovery of new nonequilibrium phases. The transitions investigated so far have been towards destroying the order of the ground state, but photoinduced phenomena in the reverse direction have been observed recently. It has been reported that the electronic order of a charge density wave,[6–8] a spin density wave,[9] superconductivity,[10–12] ferroelectricity,[13] and charge order[14–18] is enhanced by photoexcitation. We investigate one of these counterintuitive phenomena in α-(BEDT-TTF)$_2$I$_3$ (BEDT-TTF: bis[ethylenedithio]-tetrathiafulvalene).

The charge transfer salts (BEDT-TTF)$_2$X (X: a monovalent anion) can be described as quasi-two-dimensional strongly correlated electron systems with a quarter-filled valence band in the hole picture. As a result of the strong Coulomb interaction, α-(BEDT-TTF)$_2$I$_3$ exhibits charge-ordering transition. As a horizontal charge order, it has been shown to be formed below the transition temperature.[22–28,30,31] The photoinduced phase transition from the charge-ordered insulator to a metallic state has been observed in various materials by femtosecond pump-probe spectroscopy.[32–41] In α-(BEDT-TTF)$_2$I$_3$, the metallic state is generated in about 100 fs, and as many as about 250 molecules are converted to a metallic phase by one photon excitation,[32] showing the strong cooperative nature of the phenomena.

Recent pump-probe spectroscopy experiments have revealed that a short-range charge order is induced by an intense infrared pulse excitation from the metallic phase of α-(BEDT-TTF)$_2$I$_3$ just above the transition temperature,[17,18] and the localization of holes has been proposed as resulting from dynamical localization[42–44] related effect cooperated with the Coulomb interaction and the characteristic lattice structure of this compound. An electron–light coupling has been introduced into the transfer integrals as a Peierls phase, and their phases have been modulated by light excitation. If the time period of light is much smaller than the characteristic time scale of hole motion, the holes then respond approximately to the effective transfer integrals, which are given by the time average of the photo-modulated transfer integrals. For strong excitation, the effective transfer integral magnitudes are significantly reduced by light excitation, and this stabilizes the charge-ordered phase. The reduction of transfer integral has been observed as a redshift of plasmalike reflectivity edge in

$(TMTTF)_2AsF_6$ (TMTTF: tetramethyltetrathiafulvalene).[45] This proposed mechanism for the photoinduced transition is essentially different from conventional photoinduced melting of charge order. Specifically, the photoinduced melting of charge order is triggered by a real excitation, but the photoinduced charge-ordered state is a light-dressed state induced by a virtual excitation, which results in parameter modulation of the effective Hamiltonian.

There has been a rapid development on correlated systems far from equilibrium that are driven by a strong alternating current electric field.[46–51] The dynamical localization is a representative example of exotic phenomena realized in them. The dynamical localization has been originally proposed to occur under continuous light excitation.[42–44] However, the pulse duration time is long enough and the localization from the reduction of effective transfer integral magnitudes is also induced through pulse excitation in the present case. We therefore hereafter refer to the localization induced by pulse excitation as dynamical localization.

Recently, Yonemitsu has investigated the physical properties of the light-pulse excited states from the metallic ground state.[53,54] He found that the photoinduced changes in time-averaged double occupancy and intersite density-density correlations can be interpreted as arising from changes in the effective on-site and intersite repulsive interactions, respectively, relative to the transfer integrals, and that these results are consistent with experimental results. However, the photoinduced phase transition to the charge-ordered states does not occur in the excitation intensity range considered in the work. Furthermore, by analyzing not the time-averaged quantities but the dynamics of the charge-order generation, new insights into the underlying physics of the charge-ordered state are gained. The charge-ordered phase of α-(BEDT-TTF)$_2$I$_3$ is known as electronic ferroelectric.[28,29] The analysis of the dynamics also leads to an ultrafast control electric polarization.

Considering these points, we investigated the dynamics of light-pulse excited state from the metallic ground state by numerically solving the time-dependent Schrödinger equation in the quarter-filled extended Hubbard model for α-(BEDT-TTF)$_2$I$_3$. We found that the photoinduced changes in charge density mainly derive from the change in the ratio of the transfer integrals between two dominant bonds in the excitation intensity range where a precursory phenomenon for dynamical localization occurs. For intense excitation, the transition to the charge-ordered state occurs because of dynamical localization, and the photogenerated charge-ordered states can be controlled by changing the maximum amplitude and

the polarization direction of the pump pulse.

II. MODEL

For holes on a two-dimensional anisotropic triangular lattice coupled to a light field, we consider the quarter-filled extended Hubbard Hamiltonian given by

$$H(t) = \sum_{<n,m>,\sigma} \{\beta_{n,m}(t) c^{\dagger}_{n,\sigma} c_{m,\sigma} + h.c.\} + U \sum_{n} n_{n,\uparrow} n_{n,\downarrow} + \sum_{<n,m>} V_{n,m} n_n n_m. \quad (1)$$

The first term describes the hole transfer between neighbor sites, where $c^{\dagger}_{n,\sigma}$ ($c_{n,\sigma}$) creates (annihilates) a hole of spin σ at site n, $\beta_{n,m}(t)$ is the transfer integral between the sites n and m at time t, and $< n, m >$ denotes neighbor site pairs. The electron–light coupling is introduced in this term; the explicit formula for $\beta_{n,m}(t)$ is given later. The second term describes the on-site Coulomb interaction, where U is the on-site Coulomb interaction energy, and $n_{n,\sigma} = c^{\dagger}_{n,\sigma} c_{n,\sigma}$. The third term describes the Coulomb interaction between neighbor sites, where $V_{n,m}$ is the Coulomb interaction energy between the sites n and m, and $n_n = \sum_{\sigma} n_{n,\sigma}$. To take account of strong correlations, we calculate the exact dynamics of the photoexcited state on a small cluster. We consider a 4×4 cluster (system size $N = 16$) shown in Fig. 1; periodic boundary conditions are used.

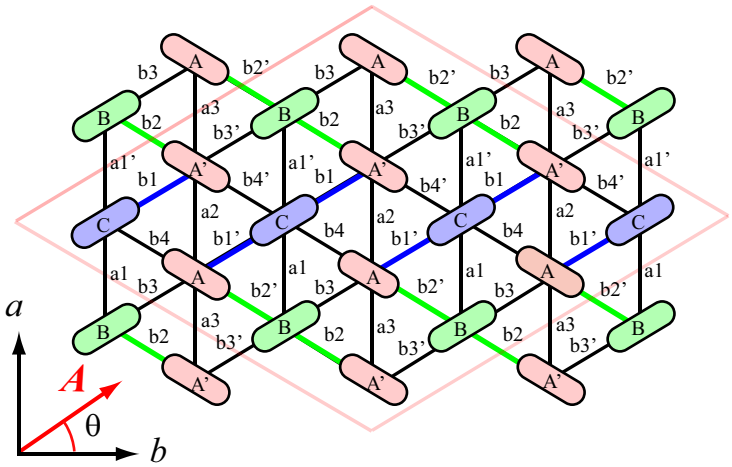

FIG. 1: (Color online) Anisotropic triangular lattices of α-(BEDT-TTF)$_2$I$_3$. The red square encloses the 4×4 cluster.

We assume the light-pulse excitation is described by a vector potential $\boldsymbol{A}(t)$ with a Gaussian profile at time t given by

$$\boldsymbol{A}(t) = \hat{\boldsymbol{A}} A^{(\max)} \exp[-(\frac{t}{D})^2] \cos(\omega t), \tag{2}$$

where $A^{(\max)}$ is the maximum amplitude, D is the pulse duration time, ω is the center frequency, and $\hat{\boldsymbol{A}}$ is the unit polarization vector.

The electron–light coupling is introduced as a Peierls phase into the transfer integrals, and $\beta_{n,m}(t)$ is given by

$$\beta_{n,m}(t) = \beta^{(0)}_{n,m} \exp[-iea A^{(\max)} \exp\{-(\frac{t}{D})^2\} \cos(\omega t) \cos(\theta - \theta_{n,m})], \tag{3}$$

where $\beta^{(0)}_{n,m}$ is the transfer integral between sites n and m when $\boldsymbol{A}(t)$ is 0, e is the elementary charge, θ ($\theta_{n,m}$) is the angle between $\hat{\boldsymbol{A}}$ ($\boldsymbol{r}_m - \boldsymbol{r}_n$) and the $b-$axis (see Fig. 1), and $\boldsymbol{r}_n$ is the position vector of site n. For simplicity, an equilateral triangle lattice of lattice spacing a is assumed.

If the period $T = 2\pi/\omega$ of the pump light photon is much smaller than the characteristic time scale of hole motion, the holes respond approximately to the effective transfer integral given by the time-average of $\beta_{n,m}(t)$,

$$\bar{\beta}_{n,m}(t) = \frac{1}{T} \int_{t-T/2}^{t+T/2} \beta_{n,m}(\tau) d\tau. \tag{4}$$

In the present case, D is much larger than T (to be shown later) and the effective transfer integral is approximately given by

$$\bar{\beta}_{n,m}(t) = \beta^{(0)}_{n,m} J_0[eaA^{(\max)} \exp\{-(\frac{t}{D})^2\} \cos(\theta - \theta_{n,m})], \tag{5}$$

where $J_0(x)$ is the Bessel function of order zero.

The function $J_0(x)$ is a decreasing function of x for $x \lesssim 4$, and $J_0(x)$ approaches zero around $x = 2.4$. Therefore, $|\bar{\beta}_{n,m}(0)|$ becomes much smaller than $|\beta^{(0)}_{n,m}|$ for strong excitations, which induces a transition from the metallic phase to the charge-ordered phase. This is the proposed mechanism of photoinduced phase transition via dynamical localization.[17,18]

The photoexcited state $|\psi(t)\rangle$ at time t is obtained by numerically solving the time-dependent Schrödinger equation with the initial condition $|\psi(-\infty)\rangle = |\phi_0\rangle$. Here $|\phi_0\rangle$ is the ground state of the electronic Hamiltonian $H_{\rm e}$, which is given by $H(t)$ for $\boldsymbol{A}(t) = 0$. We

numerically calculate $|\phi_0\rangle$ using the Lanczos method. To investigate the adiabatic nature of photoexcited state, we also consider the effective Hamiltonian $\bar{H}(t)$ given by

$$\begin{aligned}\bar{H}(t) &= \sum_{<n,m>,\sigma} \bar{\beta}_{n,m}(t)\{c^{\dagger}_{n,\sigma}c_{m,\sigma} + h.c.\} \\ &+ U\sum_{n} n_{n,\uparrow}n_{n,\downarrow} + \sum_{<n,m>} V_{n,m}n_n n_m. \end{aligned} \tag{6}$$

Here the transfer integrals $\beta_{n,m}(t)$ in $H(t)$ are replaced by effective integrals $\bar{\beta}_{n,m}(t)$. We have calculated the ground state $|\Phi_0(t)\rangle$ of $\bar{H}(t)$ using the Lanczos method.

To investigate the physical properties of the photoexcited state, we analyze the charge density $\rho_n(t)$, bond order $p_{n,m}(t)$ for $|\psi(t)\rangle$ defined by

$$\rho_n(t) = \langle\psi(t)|n_n|\psi(t)\rangle, \tag{7}$$

$$p_{n,m}(t) = \mathrm{Re}[\langle\psi(t)|\sum_{\sigma} c^{\dagger}_{n,\sigma}c_{m,\sigma}|\psi(t)\rangle]. \tag{8}$$

The bond order determines the magnitude of the bond, and is closely related to the localization of holes. If holes are localized as a result of charge-order formation, the bond orders approach zero. For the ground state $|\phi_0\rangle$, these quantities are denoted by barred symbols,

$$\bar{\rho}_n = \langle\phi_0|n_n|\phi_0\rangle, \tag{9}$$

$$\bar{p}_{n,m} = \mathrm{Re}[\langle\phi_0|\sum_{\sigma} c^{\dagger}_{n,\sigma}c_{m,\sigma}|\phi_0\rangle]. \tag{10}$$

Those for the ground state $|\Phi_0(t)\rangle$ of the effective Hamiltonian $\bar{H}(t)$ are denoted as

$$\bar{\rho}_n(t) = \langle\Phi_0(t)|n_n|\Phi_0(t)\rangle, \tag{11}$$

$$\bar{p}_{n,m}(t) = \mathrm{Re}[\langle\Phi_0(t)|\sum_{\sigma} c^{\dagger}_{n,\sigma}c_{m,\sigma}|\Phi_0(t)\rangle]. \tag{12}$$

There are four nonequivalent sites and twelve nonequivalent bonds in $H(t)$ without inversion symmetry, just as for the charge-ordered ground state with a deformed lattice structure. They are labeled as indicated in Fig. 1. The charge density $\rho_n(t)$ at the A site is denoted by $\rho_{\mathrm{A}}(t)$, and the bond order $p_{n,m}(t)$ at the b1 bond is denoted by $p_{\mathrm{b1}}(t)$. Those at the other sites or bonds, and the other quantities are denoted in the same manner. In regard to H_{e} and $\bar{H}(t)$, both have inversion symmetry, and A and A$'$ sites (Y and Y$'$ bonds, where Y=b1, b2, b3, b4, or a1) become equivalent in H_{e} and $\bar{H}(t)$. Therefore, when we refer to $\bar{\rho}_{\mathrm{X}}$, $\bar{p}_{\mathrm{Y}}$, $\bar{\rho}_{\mathrm{X}}(t)$, $\bar{p}_{\mathrm{Y}}(t)$, $\beta^{(0)}_{\mathrm{Y}}$, and $\bar{\beta}_{\mathrm{Y}}(t)$, we do not distinguish them, and both A and A$'$ sites (Y and Y$'$ bonds) are denoted as A sites (Y bonds).

In the charge-ordered states, two neighbor sites are charge-rich and the other four neighbor sites are charge-poor for every charge-rich site to minimize the Coulomb interaction energy between the neighbor sites. There are various types of charge-ordered state, which we categorize as H1, H2, D1, D2, V1, and V2 (Fig. 2), where the charge-rich and charge-poor sites are indicated using dark and light colors, respectively. The horizontal charge-ordered state where the charge-rich sites are connected by the b2, b2′, b3 and b3′ (b1, b1′, b4 and b4′) bonds is classed as H1 type (H2 type). There are two inequivalent H1-type (H2-type) charge-ordered states; see Fig. 2(a) and (b) [(c) and (d)]. There are two types of diagonal (vertical) charge-ordered states denoted by D1 and D2 types (V1 and V2 types), respectively; see Fig. 2(e) and (f) [(g) and (h)].

It is difficult to determine the type of photo-generated charge-ordered state from the charge density or the charge correlation function. Therefore, we consider the probability that all holes exist at the charge-rich sites of each type charge-ordered state. We first define $W_{\rm a}(t)$ by

$$W_{\rm a}(t) = \sum_{\sigma(1),\ldots,\sigma(8)} |\langle\psi(t)| \prod_{i=1}^{8} c^{\dagger}_{n_{\rm a}(i),\sigma(i)} |{\rm vac}\rangle|^2, \tag{13}$$

where $|{\rm vac}\rangle$ is the vacuum state, and $n_{\rm a}(i)$ for $i = 1, \ldots, 8$ are the site numbers of eight charge-rich sites of the charge-ordered state shown in Fig. 2(a). The weights $W_{\rm b}(t)$, ..., and $W_{\rm h}(t)$ are defined in the same way. The probability of the H1-type charge-ordered state $W_{\rm H1}(t)$ is given by $W_{\rm H1}(t) = 2W_{\rm a}(t) + 2W_{\rm b}(t)$. The A and B sites are charge-rich and the A′ and C sites are charge-poor in the charge-ordered state shown in Fig. 2(a). There is an equivalent charge-ordered state to this one, where the A′ and B sites are charge-rich and the A and C sites are charge-poor. There is also an equivalent charge-ordered state to that shown in 2(b). The factor 2 comes from these equivalent states. In the same way, we obtain $W_{\rm H2}(t) = 2W_{\rm c}(t) + 2W_{\rm d}(t)$, $W_{\rm D1}(t) = 2W_{\rm e}(t)$, $W_{\rm D2}(t) = 2W_{\rm f}(t)$, $W_{\rm V1}(t) = W_{\rm g}(t)$, and $W_{\rm V2}(t) = W_{\rm h}(t)$. We further consider the sum $W_{\rm tot}(t) = W_{\rm H1}(t) + W_{\rm H2}(t) + W_{\rm D1}(t) + W_{\rm D2}(t) + W_{\rm V1}(t) + W_{\rm V2}(t)$ over all the charge-order types.

III. RESULTS

We adopt the transfer integrals deduced from the extended Hückel calculation: $\beta^{(0)}_{\rm a1} = 0.035$, $\beta^{(0)}_{\rm a2} = 0.0461$, $\beta^{(0)}_{\rm a3} = -0.0181$, $\beta^{(0)}_{\rm b1} = -0.1271$, $\beta^{(0)}_{\rm b2} = -0.1447$, $\beta^{(0)}_{\rm b3} = -0.0629$,

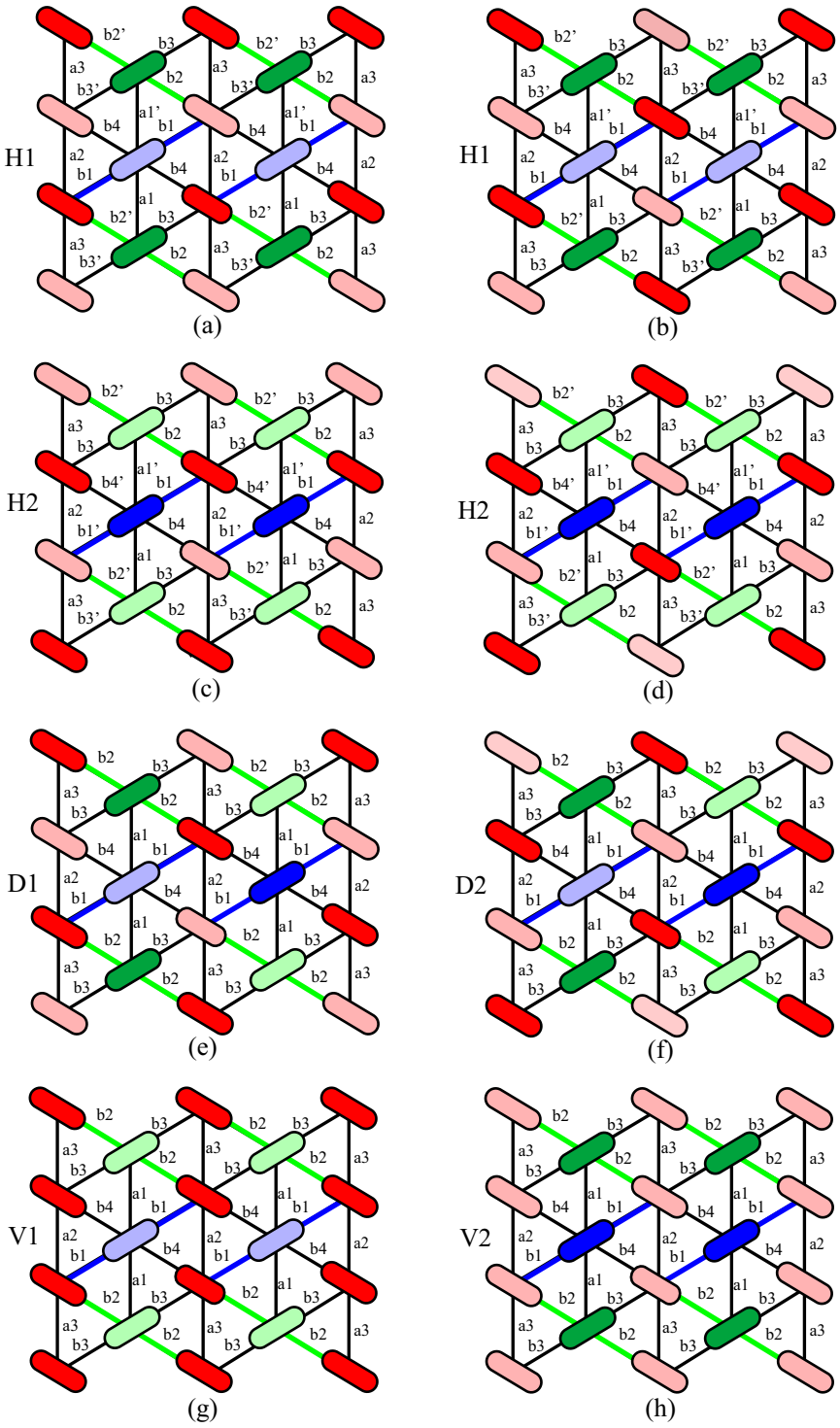

FIG. 2: (Color online) The charge structures of two inequivalent H1-type charge-ordered states [(a) and (b)], of two inequivalent H2-type charge-ordered states [(c) and (d)], and those of D1, D2, V1, and V2 type charge-ordered states [(e), (f), (g), and (h), respectively]. A and A′ sites are marked by red ovals, B and C sites by blue and green ovals, respectively, and charge-rich (charge-poor) sites by dark-color (light-color) ovals.

and $\beta_{\rm b4}^{(0)} = -0.0245$.[27] Hereinafter, we use eV as the unit of energy and eV^{-1} as the unit of time, where 1 eV^{-1} equals 0.658 fs. We adopt the following Coulomb parameters: U =0.9, $V_{\rm V}$ =0.22, and $V_{\rm D}$ =0.18, where $V_{n,m} = V_{\rm V}$ ($V_{\rm D}$) if the neighbor site pair $< n, m >$ is on the vertical (diagonal) bonds. This set of parameters reproduces well the charge densities obtained from experiments. The calculated charge densities for the metallic ground state (the experimentally obtained charge densities in the metallic phase[27]) are: $\bar{\rho}_{\rm A}$ =0.53 (0.49), $\bar{\rho}_{\rm B}$ =0.53 (0.57), and $\bar{\rho}_{\rm C}$ =0.42 (0.41).

As a result of strong Coulomb interaction, the sum of the weights for the metallic ground state $\bar{W}_{\rm tot} = 1.1 \times 10^{-2}$ is much larger than that $\bar{W}_{\rm tot}({\rm FH}) = 1.1 \times 10^{-3}$ for free holes, where holes are distributed randomly. We have calculated the ground state of charge-ordered phase, which reproduces the experimentally obtained charge densities very well.[52] In the charge-ordered ground state, the weight of the H1-type charge ordered state $\bar{W}_{\rm H1}({\rm CO}) = 4.3 \times 10^{-2}$ is slightly smaller than the sum of the weights $\bar{W}_{\rm tot}({\rm CO}) = 4.8 \times 10^{-2}$, and the H1-type charge-ordered state has dominant weight. The weight $\bar{W}_{\rm tot}({\rm CO})$ can be regarded as the criterion for charge-order generation; it is much smaller than unity because of charge fluctuations, and that $\bar{W}_{\rm tot}$ for the metallic ground state is much smaller than $\bar{W}_{\rm tot}({\rm CO})$.

As for the light pulse parameters, we adopt the pulse duration time $D = 60$, where the full-width at half-maximum (66 fs) is much larger than that used in the experiment (7 fs), and the center frequency $\omega = 2$, which is much larger than that used in experiment (0.9). This is because dynamical localization clearly occurs with these parameters under intense excitation. How the results depend on these parameters will be discussed later.

A. Precursory phenomena for dynamical localization

We show the results for $eaA^{(\max)} = 1$ in this section. The magnitude is comparable with that used in experiment, and precursory phenomena for dynamical localization were observed as we shall describe later. We show the time variation of $\rho_{\rm X}(t)$ (X=A, B, and C), $p_{\rm Y}(t)$ (Y=b1, b2, b3, b4, a1, a2, and a3) and $W_{\rm Z}(t)$ (Z=H1, H2, D1, D2, V1, V2, and tot) for $\theta = -50^\circ$ and those for $\theta = 50^\circ$ in Figs. 3 and 4, respectively. In these figures, $\rho_{\rm X}(t)$ are strongly changed by photoexcitation. The charge density $\rho_{\rm X}(t)$ and the bond order $p_{\rm Y}(t)$ can be decomposed into a slow-varying component and rapidly oscillating component with frequency ω; the latter component is significant in $\rho_{\rm A}(t)$ and $\rho_{\rm A'}(t)$ but is small in other

quantities. Because the slow-varying components of $\rho_{\rm A}(t)$ and $\rho_{\rm A'}(t)$ ($p_{\rm Y}(t)$ and $p_{\rm Y'}(t)$) are the same, and the corresponding rapidly oscillating components have opposite phase in all instances considered, we only show $\rho_{\rm A}(t)$ ($p_{\rm Y}(t)$) in the figures that following.

We also show the charge density $\bar{\rho}_{\rm X}(t)$ and the bond order $\bar{p}_{\rm Y}(t)$ for the ground state of the effective Hamiltonian $\bar{H}(t)$ at $t = \pm 60$, ± 50, ± 40, ± 30, ± 20, ± 10, and 0 in Figs. 3 and 4. These figures show that the slow-varying components of $\rho_{\rm X}(t)$ ($p_{\rm Y}(t)$) roughly agree with $\bar{\rho}_{\rm X}(t)$ ($\bar{p}_{\rm Y}(t)$). We conclude therefore that the photoexcited state $|\psi(t)\rangle$ changes nearly adiabatically with the time variation of effective transfer integrals $\bar{\beta}_{n,m}(t)$ during the light pulse excitation. The peaks of the photoinduced changes in these quantities are delayed from the pulse peak by about 20 for $\theta = 50°$; the delay is negligible for $\theta = -50°$. This shows that the time scale for hole motion is comparable or slightly larger than D.

The temporal profiles of $\rho_{\rm X}(t)$ and $p_{\rm Y}(t)$ for $\theta = -50°$ are quite different from those for 50°. We here consider the origin of the strong θ dependence of the photoinduced dynamics. For this purpose, we first consider the origin of charge disproportionation in the metallic ground state. Even in the metallic phase, the charge density is not uniform, and $\bar{\rho}_{\rm B}$ is significantly larger than $\bar{\rho}_{\rm C}$. The charge disproportionation arises from the anisotropy in $\beta_{\rm Y}^{(0)}$. The absolute value $|\beta_{\rm Y}^{(0)}|$ is the largest for the b2 bond and the second largest for the b1 bond; they are much larger than those for other bonds. From Eq. (1), the energy gain arising from the formation of Y bond is given by $-\beta_{\rm Y}^{(0)}\bar{p}_{\rm Y}$. To maximize the energy gain, $\bar{p}_{\rm Y}$ is also the largest for the b2 bond and the second largest for the b1 bond. In Fig. 1, the strongest b2 bonds are drawn in green, the second strongest b1 bonds are drawn in blue, and the B (C) site is connected by two b2 (b1) bonds. Because holes that contribute to stronger bonds are more stable, $\bar{\rho}_{\rm B}$ becomes significantly larger than $\bar{\rho}_{\rm C}$. The charge disproportionation in the metallic ground state $|\phi_0\rangle$ can be understood from the ratio of $|\beta_{\rm b1}^{(0)}|$ to $|\beta_{\rm b2}^{(0)}|$. Furthermore, as the A site is connected by one b2 bond and one b1 bond, $\bar{\rho}_{\rm A}$ is nearly independent of the ratio. The importance of anisotropy of the transfer integrals in the charge distribution has been pointed out in several previous works.[55,56]

Next, we consider the charge disproportionation in $|\Phi_0(t)\rangle$, which is also the metallic ground state of the effective Hamiltonian $\bar{H}(t)$. From this, we can understand the origin of the photoinduced dynamics because of the adiabatic nature of $|\psi(t)\rangle$. At $\theta = -50°$, $\cos(\theta - \theta_{\rm b2}) \gg \cos(\theta - \theta_{\rm b1})$ holds, and the photoinduced reduction in $|\bar{\beta}_{\rm b2}(t)|$ is much larger than that in $|\bar{\beta}_{\rm b1}(t)|$ as indicated by Eq. (5). As a result, $|\bar{\beta}_{\rm b1}(t)|$ becomes larger than $|\bar{\beta}_{\rm b2}(t)|$

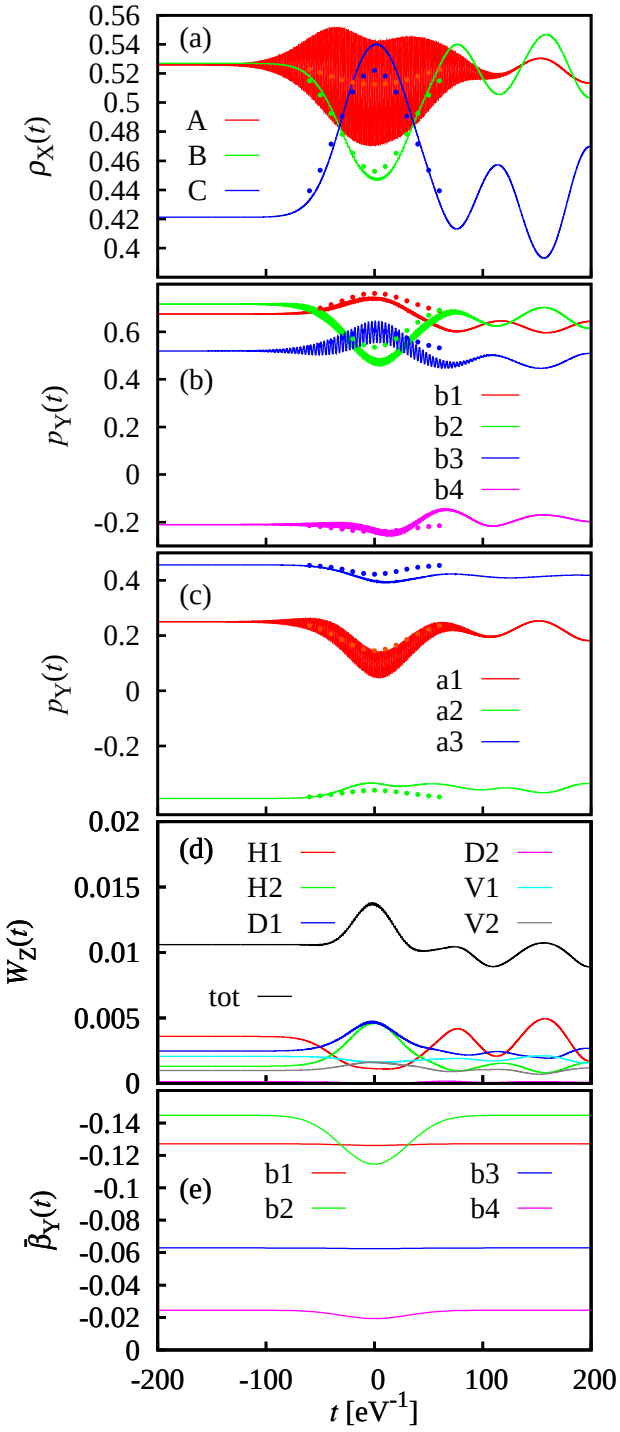

FIG. 3: (Color online) Time variation of (a) $\rho_{\rm X}(t)$ (solid lines) and $\bar{\rho}_{\rm X}(t)$ (dotted curves), (b) $p_{\rm Y}(t)$ (solid lines) and $\bar{p}_{\rm Y}(t)$ (dotted curves) for diagonal bonds, (c) $p_{\rm Y}(t)$ (solid lines) and $\bar{p}_{\rm Y}(t)$ (dotted curves) for vertical bonds, (d) $W_{\rm Z}(t)$, and (e) $\bar{\beta}_{\rm Y}(t)$, for $eaA^{(\rm max)} = 1$, $\theta = -50°$, and $D = 60$.

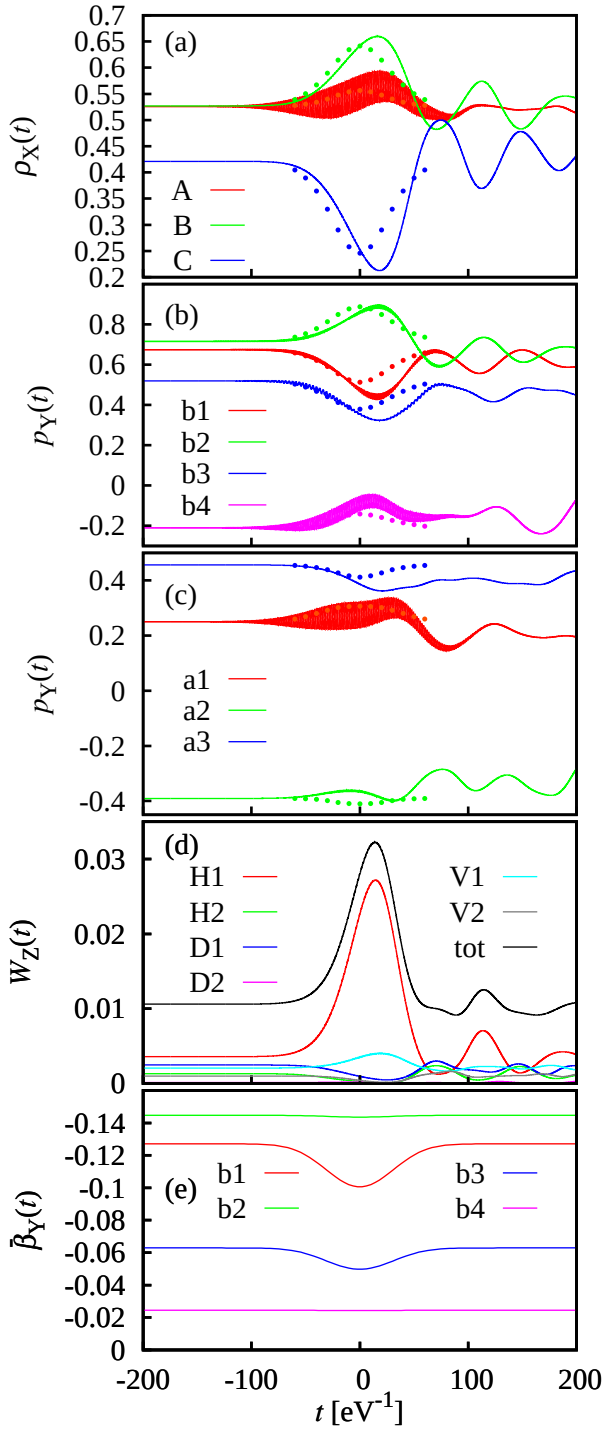

FIG. 4: (Color online) Time variation of (a) $\rho_{\rm X}(t)$ (solid lines) and $\bar{\rho}_{\rm X}(t)$ (dotted curves), (b) $p_{\rm Y}(t)$ (solid lines) and $\bar{p}_{\rm Y}(t)$ (dotted curves) for diagonal bonds, (c) $p_{\rm Y}(t)$ (solid lines) and $\bar{p}_{\rm Y}(t)$ (dotted curves) for vertical bonds, (d) $W_{\rm Z}(t)$, and (e) $\bar{\beta}_{\rm Y}(t)$, for $eaA^{(\max)} = 1$, $\theta = 50^\circ$, and $D = 60$.

for $-30 \lesssim t \lesssim 30$ [Fig. 3(e)]. In the time interval where magnitude reversal occurs, $\bar{p}_{\rm b1}(t)$ becomes larger than $\bar{p}_{\rm b2}(t)$, and the C (B) site becomes charge-rich (charge-poor) in $|\Phi_0(t)\rangle$ [Fig. 3(a) and (b)]. In contrast to this, the slow-varying component of $\bar{\rho}_{\rm A}(t)$ stays nearly constant all through the time interval. These results show that the charge disproportionation in $|\Phi_0(t)\rangle$ is determined mainly from the ratio between $|\bar{\beta}_{\rm b1}(t)|$ and $|\bar{\beta}_{\rm b2}(t)|$.

At $\theta = 50°$, $\cos(\theta - \theta_{\rm b1}) \gg \cos(\theta - \theta_{\rm b2})$ holds, and the reduction in $|\bar{\beta}_{\rm b1}(t)|$ from photoexcitation is much larger than that in $|\bar{\beta}_{\rm b2}(t)|$ [Fig. 4(e)]. As a result, $\bar{p}_{\rm b2}(t)/\bar{p}_{\rm b1}(t)$ becomes significantly larger than $\bar{p}_{\rm b2}/\bar{p}_{\rm b1}$, and $\bar{\rho}_{\rm B}(t) - \bar{\rho}_{\rm C}(t)$ becomes significantly larger than $\bar{\rho}_{\rm B} - \bar{\rho}_{\rm C}$ during excitation by the light pulse [Fig. 4(a) and (b)]. The charge disproportionation in $|\Phi_0(t)\rangle$ is determined mainly from the ratio also at $\theta = 50°$.

To investigate the polarization angle dependence of photoinduced dynamics in more detail, we considered the charge density $\rho_{\rm X}^{(\max)}$ when the deviation from that of the ground state becomes largest. Specifically, $\rho_{\rm X}^{(\max)}$ is defined by $\rho_{\rm X}^{(\max)} = \rho_{\rm X}(t_{\max})$, where $|\rho_{\rm X}(t) - \bar{\rho}_{\rm X}|$ becomes largest at $t = t_{\max}$, for X=B and C. For $\rho_{\rm A}^{(\max)}$, we considered the average charge density over the sites A and A$'$ defined as $\rho_{\rm A}^{(\max)} = \{\rho_{\rm A}(t_{\max}) + \rho_{\rm A'}(t_{\max})\}/2$, where $|\{\rho_{\rm A}(t) + \rho_{\rm A'}(t)\}/2 - \bar{\rho}_{\rm A}|$ becomes largest at $t = t_{\max}$. Because the phase of the rapidly oscillating components of $\rho_{\rm A}(t)$ is opposite to that of $\rho_{\rm A'}(t)$, the average is their slow-varying component. At $\theta = -50°$ ($50°$), $t_{\max} \simeq 0$ (20) for all these values; see Fig. 3(a) (Fig. 4(a)).

We present the θ dependence of $\rho_{\rm X}^{(\max)}$ and the effective transfer integral $\bar{\beta}_{\rm Y}(0)$ at the peak of the light pulse in Fig. 5(a) and (c), respectively. For $-70° \lesssim \theta \lesssim -20°$, where $|\bar{\beta}_{\rm b1}(0)|$ is larger than $|\bar{\beta}_{\rm b2}(0)|$, $\rho_{\rm C}^{(\max)}$ becomes larger than $\rho_{\rm B}^{(\max)}$. The charge distribution in the region results from the magnitude reversal as evident when $\theta = -50°$. For $20° \lesssim \theta \lesssim 80°$, where the ratio $|\bar{\beta}_{\rm b2}(0)|/|\bar{\beta}_{\rm b1}(0)|$ is significantly larger than $|\beta_{\rm b2}^{(0)}|/|\beta_{\rm b21}^{(0)}|$, $\rho_{\rm B}^{(\max)} - \rho_{\rm C}^{(\max)}$ becomes significantly larger than $\bar{\rho}_{\rm B} - \bar{\rho}_{\rm C}$. The charge distribution in the region results from the photoinduced increase in the ratio $|\bar{\beta}_{\rm b2}(t)|/|\bar{\beta}_{\rm b1}(t)|$ as obtained for $\theta = 50°$. Despite the significant change in the ratio, $\rho_{\rm A}^{(\max)}$ is nearly constant with θ. From these results, we conclude that photoinduced dynamics is mainly driven by the change of the ratio $|\bar{\beta}_{\rm b2}(t)|/|\bar{\beta}_{\rm b1}(t)|$ throughout the θ region, and the characteristic θ dependence of the dynamics can be explained from the θ dependence of the ratio.

We also consider $W_{\rm Z}^{(\max)}$, which is the maximum value of $W_{\rm Z}(t)$, and show the θ dependence of $W_{\rm Z}^{(\max)}$ in Fig. 5(b). Around $\theta = 50°$, photoexcitation increases $W_{\rm tot}$ nearly 3-fold. However, $W_{\rm Z}^{(\max)}$ is significantly smaller than that $\bar{W}_{\rm tot}({\rm CO})$ of the charge-ordered

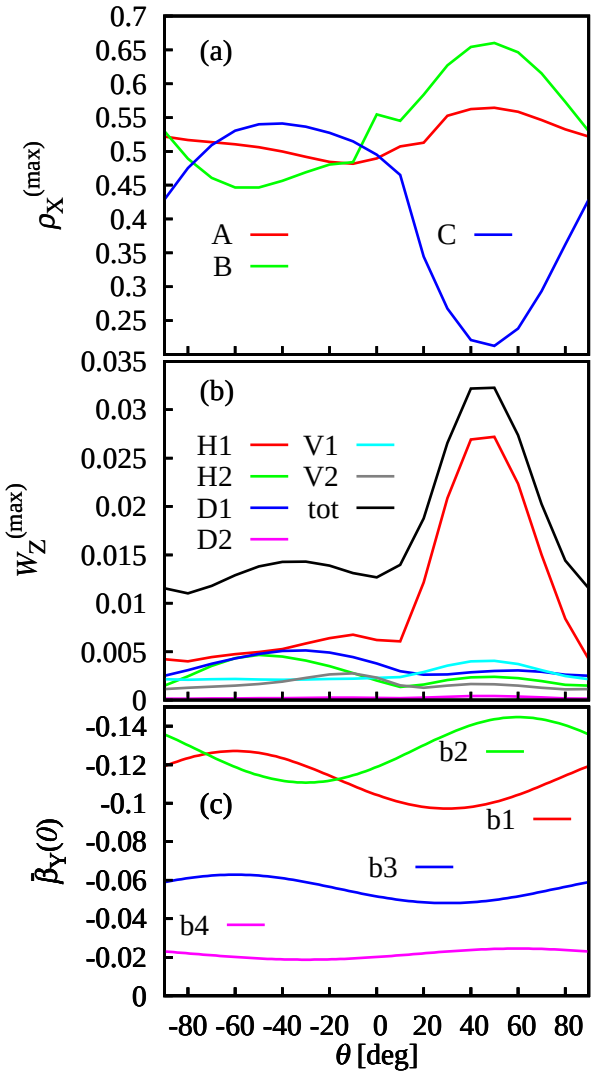

FIG. 5: (Color online) The θ dependence of (a) $\rho_{\rm X}^{(\rm max)}$, (b) $W_{\rm Z}^{(\rm max)}$, and (c) $\bar{\beta}_{\rm Y}(0)$, for $eaA^{(\rm max)} = 1$ and $D = 60$.

ground state. Furthermore, the ratio $|p_{\rm b2}(t)|/|p_{\rm b1}(t)|$ is largely changed by photoexcitation, but overall the reduction in $|p_{\rm Y}(t)|$ is not seen in Fig. 3(b) and (c), and Fig. 4(b) and (c), which show that holes are not localized in this instance. Therefore, the large photoinduced change in charge density for $eaA^{(\rm max)} = 1$ is not because of dynamical localization but from a photoinduced change in the ratio between $|\bar{\beta}_{\rm b1}(t)|$ and $|\bar{\beta}_{\rm b2}(t)|$.

The duration time $D = 60$ used to obtain these results, is much larger than that used in experiments. We have numerically calculated the dynamics using different duration times $D = 10$ and 300. The full-width at half-maximum for $D = 10$ is equal to 11 fs, and is about

the same as that used in the experiment (7 fs). We show in Fig. 6 the time variation of $\rho_{\rm X}(t)$, $\bar{\rho}_{\rm X}(t)$ and $W_{\rm Z}(t)$ for $\theta = 50^\circ$ when the duration time $D = 10$ is used. The photoinduced dynamics for $D = 10$ under pump light excitation is basically the same as that for $D = 60$ except the photoinduced changes of $\rho_{\rm B}(t)$ and $\rho_{\rm C}(t)$ are much smaller than encountered in the latter. Therefore, the photoinduced charge dynamics is driven by the photoinduced change in the ratio between $|\bar{\beta}_{\rm b1}(t)|$ and $|\bar{\beta}_{\rm b2}(t)|$ also for $D = 10$. Much smaller changes of $\rho_{\rm B}(t)$ and $\rho_{\rm C}(t)$ can be attributed to the fact that the time scale of hole motion, which is comparable or slightly larger than 60 as fore-mentioned, is much larger than D. In this case, the light pulse decays before the charge distribution for the adiabatic state $|\Phi_0(0)\rangle$ at the peak of the pulse is generated, and therefore photoinduced changes of $\rho_{\rm B}(t)$ and $\rho_{\rm C}(t)$ become much smaller. This can be confirmed from the significant deviation between $\rho_{\rm B}(t)$ and $\bar{\rho}_{\rm B}(t)$ and between $\rho_{\rm C}(t)$ and $\bar{\rho}_{\rm C}(t)$.

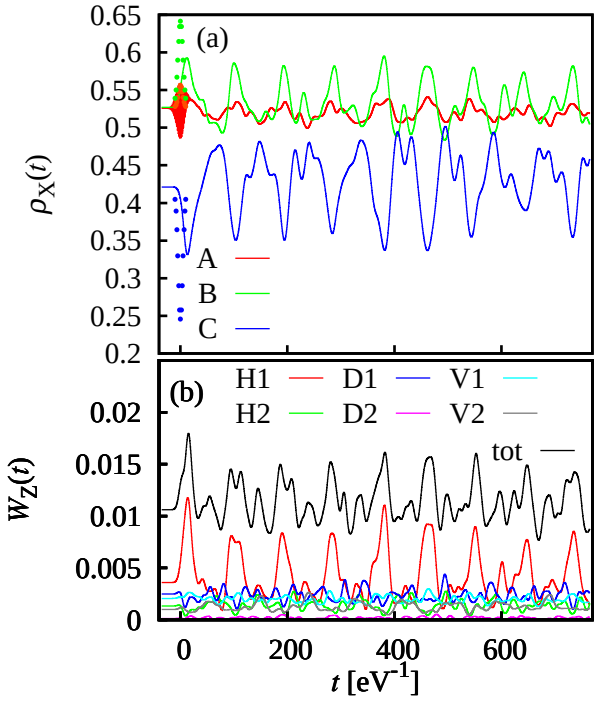

FIG. 6: (Color online) Time variation of (a) $\rho_{\rm X}(t)$ (solid lines) and $\bar{\rho}_{\rm X}(t)$ (dotted curves), and (b) $W_{\rm Z}(t)$, for $eaA^{(\max)} = 1$, $\theta = 50^\circ$, and $D = 10$.

In the time interval after the pump pulse has decayed, $\rho_{\rm B}(t)$, $\rho_{\rm C}(t)$ and $W_{\rm tot}(t)$ exhibit complicated oscillations. To investigate the origin of these characteristic oscillations, we have calculated the discrete Fourier transformations $\mathcal{F}[\rho_{\rm X}](E_j)$ ($\mathcal{F}[W_{\rm Z}](E_j)$) of $\rho_{\rm X}(t)$ ($W_{\rm Z}(t)$)

defined by

$$\mathcal{F}[\rho_{\rm X}](E_j) = \sum_{l=1}^{L} \rho_{\rm X}(t_l) \exp[iE_j t_l], \tag{14}$$

where $t_l = t_0 + \Delta t l$, $t_0 = 40$, $\Delta t = 0.03$, $L = 24000$, $E_j = (2\pi/T_{\rm FT})j$, $T_{\rm FT} = \Delta t L$, and j is an integer in the range $-L/2 < j \leq L/2$. We considered the polarization directions $\theta = -50°$, $-10°$ and $50°$, where quite different photoinduced dynamics are seen. We show E_j dependence of $|\mathcal{F}[\rho_{\rm B}](E_j)|$ and $|\mathcal{F}[\rho_{\rm C}](E_j)|$ for $\theta = 50°$ [Fig. 7(a)], and that of $|\mathcal{F}[W_{\rm tot}](E_j)|$ for $\theta = -50°$, $-10°$ and $50°$ [Fig. 7(b)].

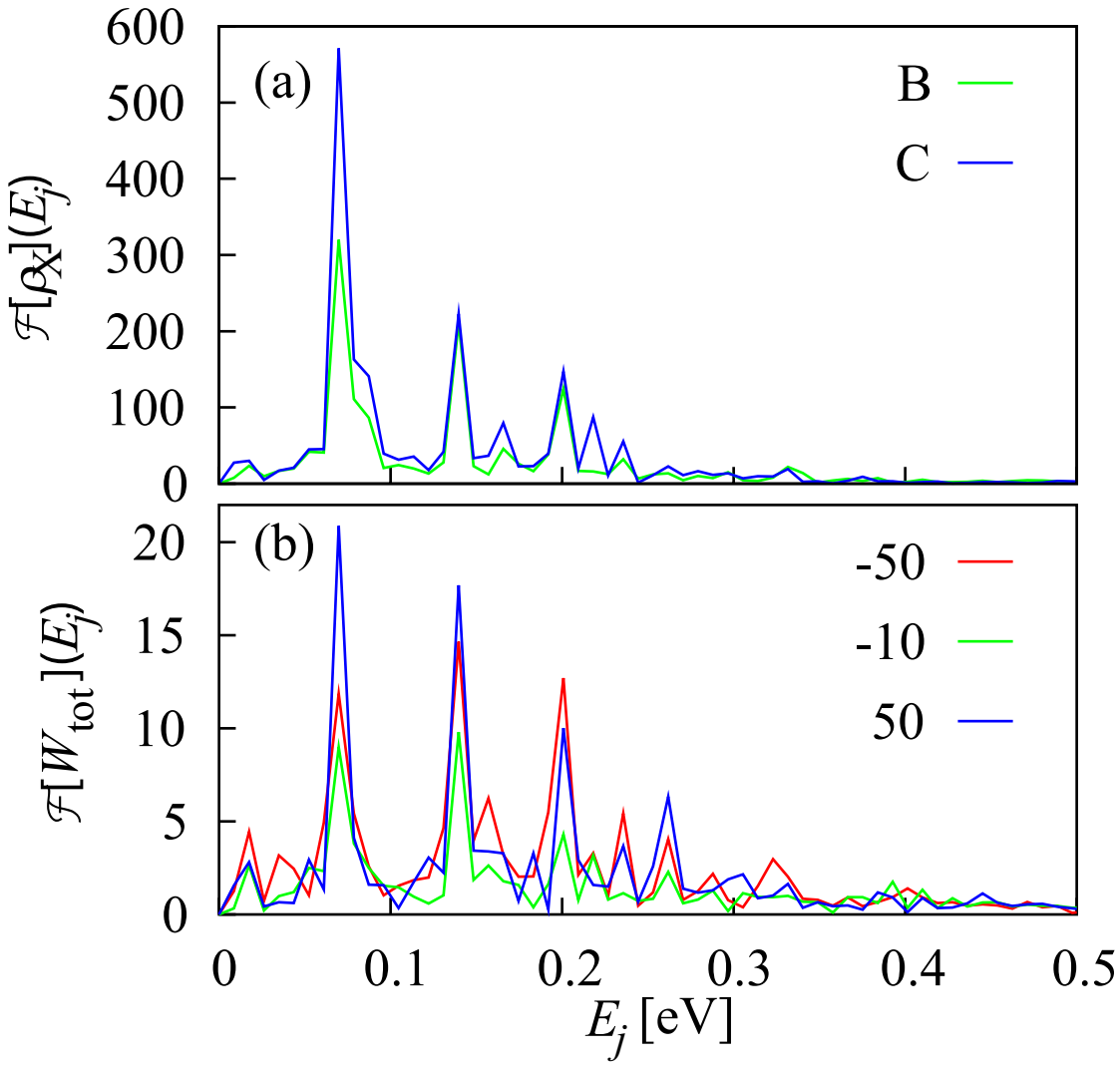

FIG. 7: (Color online) The E_j dependence of (a) $|\mathcal{F}[\rho_{\rm B}](E_j)|$ and $|\mathcal{F}[\rho_{\rm C}](E_j)|$ for $\theta = 50°$, and (b) that of $|\mathcal{F}[W_{\rm tot}](E_j)|$ for $\theta = -50°$, $-10°$ and $50°$. The maximum amplitude $eaA^{(\rm max)} = 1$ and the duration time $D = 10$ are used.

As seen from this figure, there are large peaks at $E_j = 0.070$, 0.14 and 0.20 eV for all these quantities, and the peak energies are almost independent of θ despite the strong θ dependence of the photoinduced dynamics; only their absolute values and phases at peak energies depend strongly on θ. This shows that there are three collective modes that dominate the dynamics after the pump pulse has decayed. Time variations of the bond orders $p_{\rm b2}(t)$ and $p_{\rm b1}(t)$ for the two strongest bonds and the charge density oscillations are strongly coupled in the collective mode similar to when the pump pulse is on; that is, $\rho_{\rm B}(t)$ ($\rho_{\rm C}(t)$) becomes larger when $p_{\rm b2}(t)/p_{\rm b1}(t)$ becomes larger (smaller). The probability $W_{\rm tot}(t)$ becomes significantly larger than $\bar{W}_{\rm tot}$ around the time when $|\rho_{\rm B}(t)-\bar{\rho}_{\rm B}|$ and $|\rho_{\rm C}(t)-\bar{\rho}_{\rm C}|$ exhibit a local maximum. Therefore, these collective modes are closely related to the charge order generation.

These oscillations come from a deviation from adiabatic motion. When D is significantly smaller than the time scale of hole motion, the holes cannot follow the time variation of the effective Hamiltonian $\bar{H}(t)$ adiabatically, which induces these collective motions. Actually, the amplitudes of these oscillations in the time interval are largest for $D = 10$, and the oscillations are almost negligible for $D = 300$, where the pulse excited state $|\psi(t)\rangle$ changes almost adiabatically with $\bar{H}(t)$.

B. Dynamical localization

We now show the results for $eaA^{(\max)} = 2.3$, where the dynamical localization is observed clearly, as will be demonstrated. We show the time variation of $\rho_{\rm X}(t)$, $\bar{\rho}_{\rm X}(t)$, $p_{\rm Y}(t)$, $\bar{p}_{\rm Y}(t)$, $W_{\rm Z}(t)$, and $\bar{\beta}_{\rm Y}(t)$, for $\theta = -10^\circ$ and 50° in Figs. 8 and 9, respectively.

With the present strong pulse, the effective transfer integrals diminish significantly. For $\theta = -10^\circ$, $|\bar{\beta}_{\rm Y}(t)|/|\beta_{\rm Y}^{(0)}|$ for b2 and b4 (b1 and b3) bonds are reduced to 0.13 (0.36) at the peak time of the light pulse. As a result, $|p_{\rm X}(t)|$ for all the b bonds decrease significantly around $t = 0$, indicating that a hole becomes much more localized at a charge-rich site. Furthermore, the total weight of the charge-ordered states $W_{\rm tot}(t)$ is increased by about 30 times and becomes much larger than that for the charge-ordered ground state. These results show that charge order is photo-generated in this instance.

For $\theta = 50^\circ$, $|\bar{\beta}_{\rm b1}(t)|/|\beta_{\rm b1}^{(0)}|$ is reduced significantly to 0.13 but the reduction in $|\bar{\beta}_{\rm b2}(t)|/|\beta_{\rm b2}^{(0)}|$ is 0.96 at the peak time of the light pulse. As a result, $p_{\rm b2}(t)$ and $p_{\rm b2'}(t)$ become even larger than $\bar{p}_{\rm b2}$ but $p_{\rm X}(t)$ for the other bonds approach zero around $t = 0$. This

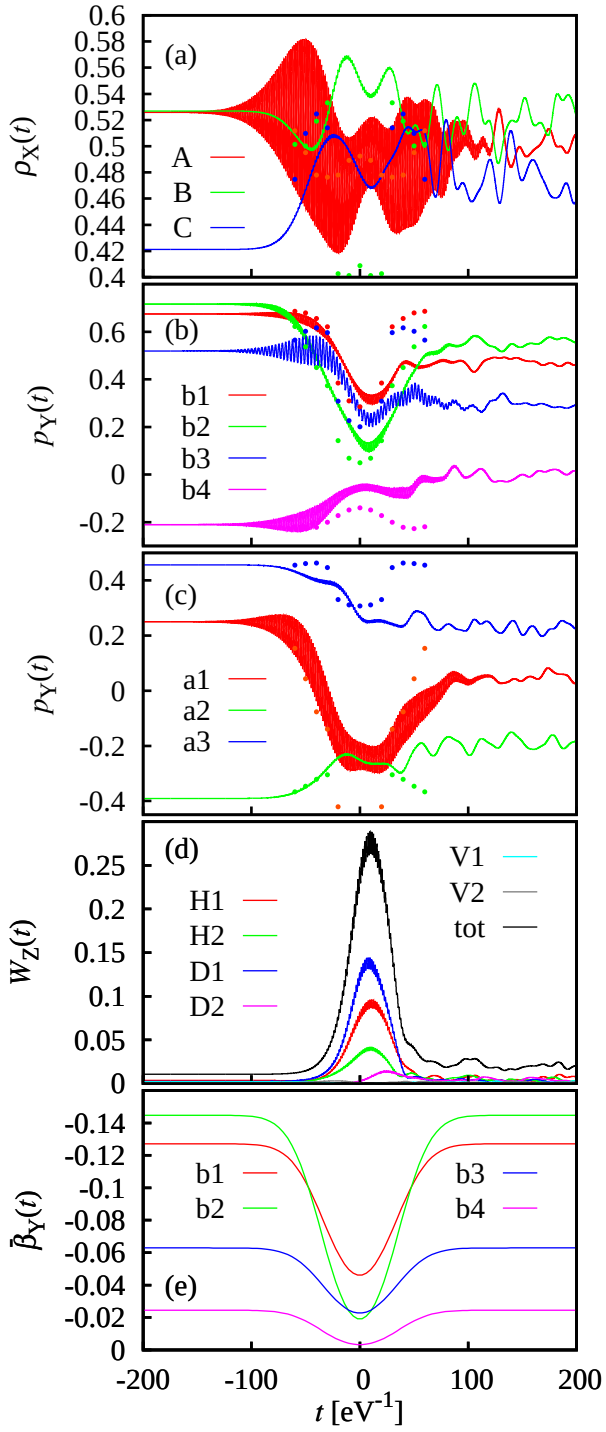

FIG. 8: (Color online) Time variation of (a) $\rho_{\rm X}(t)$ (solid lines) and $\bar{\rho}_{\rm X}(t)$ (dotted curves), (b) $p_{\rm Y}(t)$ (solid lines) and $\bar{p}_{\rm Y}(t)$ (dotted curves) for diagonal bonds, (c) $p_{\rm Y}(t)$ (solid lines) and $\bar{p}_{\rm Y}(t)$ (dotted curve) for vertical bonds, (d) $W_{\rm Z}(t)$, and (e) $\bar{\beta}_{\rm Y}(t)$, for $eaA^{(\rm max)} = 2.3$, $\theta = -10^\circ$, and $D = 60$.

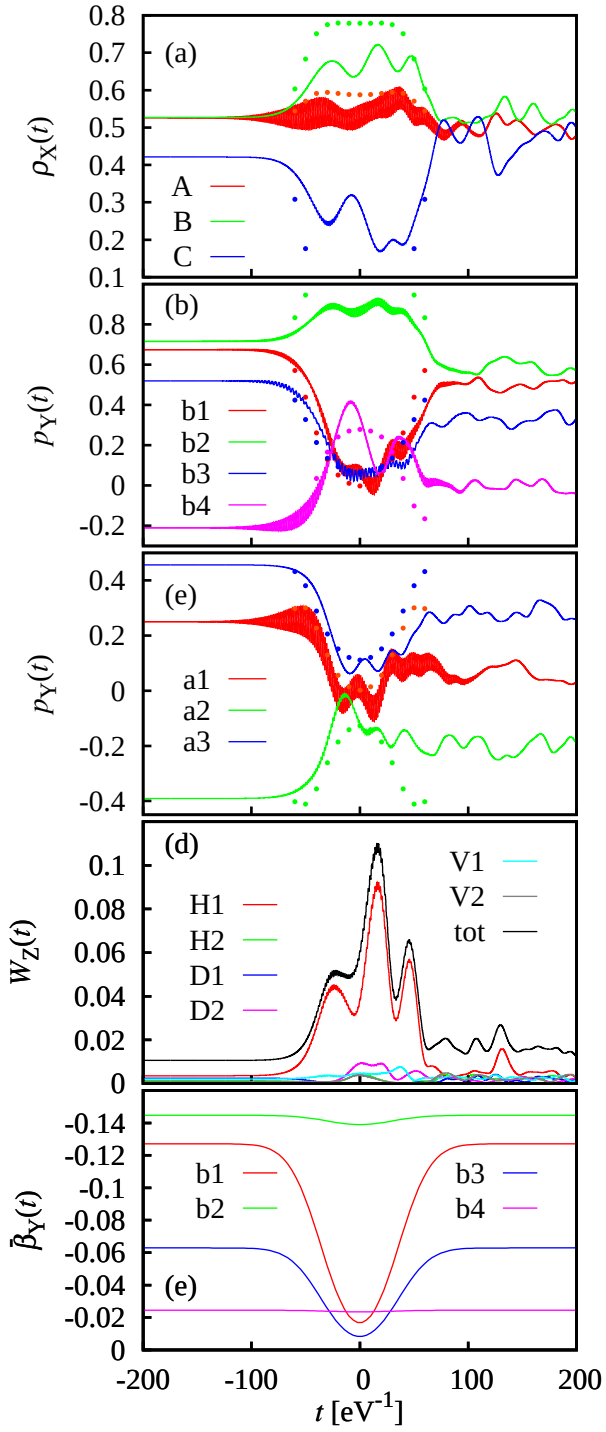

FIG. 9: (Color online) Time variation of (a) $\rho_X(t)$ (solid lines) and $\bar{\rho}_X(t)$ (dotted curves), (b) $p_Y(t)$ (solid lines) and $\bar{p}_Y(t)$ (dotted curves) for diagonal bonds, (c) $p_Y(t)$ (solid lines) and $\bar{p}_Y(t)$ (dotted curves) for vertical bonds, (d) $W_Z(t)$, and (e) $\bar{\beta}_Y(t)$, for $eaA^{(\max)} = 2.3$, $\theta = 50°$, and $D = 60$.

shows that holes are localized on the b2 bonds. The weight $W_{\rm tot}(t)$ is increased by about 10 times and becomes much larger than that for the charge-ordered ground state. Furthermore, $W_{\rm H1}(t)$ is much larger than $W_{\rm Z}(t)$ for the other charge-order types. These results show that the H1-type charge order is photo-generated in this instance. This contrasts with the situation when $\theta = -10°$, for which $W_{\rm D1}(t)$ and $W_{\rm H1}(t)$ are comparable.

Under the intense excitation, deviations of $\rho_{\rm X}(t)$ from $\bar{\rho}_{\rm X}(t)$ and those of $p_{\rm Y}(t)$ from $\bar{p}_{\rm Y}(t)$ are significant, showing that $|\psi(t)\rangle$ does not change adiabatically with $H(t)$. However, the characteristic photoinduced dynamics from an intense excitation is also induced by the change in $\bar{\beta}_{\rm Y}(t)$. We confirmed this by calculating the photoinduced dynamics using different ω. For $\omega \gtrsim 2$, $\rho_{\rm X}(t)$, $p_{\rm Y}(t)$ and $W_{\rm Z}(t)$ are nearly independent of ω except for the rapidly oscillating components with frequency ω. Note that the effective transfer integrals given by Eq. (4) do not depend on ω. This very weak ω dependence is the characteristic feature of the dynamics in the higher-frequency off-resonance case, which is induced by the change in the effective transfer integrals. The photoinduced dynamics is induced by a virtual excitation, which changes the effective transfer integrals. Therefore, the photo-generated charge-ordered states can be regarded as a light-dressed state.

The photoinduced dynamics for $\theta = -10°$ and that for $\theta = 50°$ are quite different. To see the θ dependence of the photoinduced dynamics in more detail, we present the θ dependence of $\rho_{\rm X}^{(\rm max)}$ and $W_{\rm Z}^{(\rm max)}$ in Fig. 10. The maximum value $W_{\rm tot}^{(\rm max)}$ and $W_{\rm Z}^{(\rm max)}$ strongly depend on θ, and $W_{\rm tot}^{(\rm max)}$ is larger than that of the charge-ordered ground state; the charge order is photo-generated except for the narrow region near $\theta = \pm 90°$.

We here consider the origin of their strong θ dependence. In the strong interaction limit, where transfer term is neglected, the horizontal and diagonal charge-ordered states are degenerate in energy. Because $V_{\rm V}$ is larger than $V_{\rm D}$, the vertical charge-ordered states have larger Coulomb interaction energies than the horizontal and diagonal charge-ordered states. As a result, $W_{\rm V1}^{(\rm max)}$ and $W_{\rm V2}^{(\rm max)}$ are much smaller than those of the other charge-ordered states. We therefore focus on the horizontal and diagonal charge-ordered states in the following.

The degeneracy between the horizontal and diagonal charge-ordered states is lifted by introducing the transfer term.[56] Bonds are formed between the neighboring sites as a result of charge fluctuations induced by the transfer term, even in the charge-ordered states. In the following, a bond that connects two charge-rich (charge-poor) sites is denoted by a 1-1

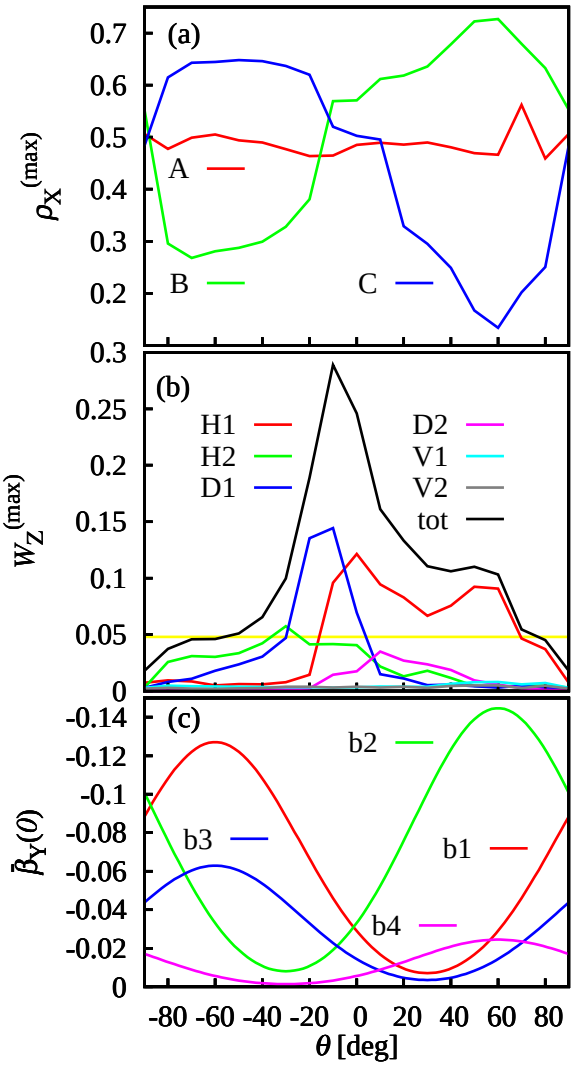

FIG. 10: (Color online) The θ dependence of (a) $\rho_{\rm X}^{(\rm max)}$, (b) $W_{\rm Z}^{(\rm max)}$, and (c) $\bar{\beta}_{\rm Y}(0)$ for $eaA^{(\rm max)} = 2.3$ and $D = 60$. The horizontal line shows $\bar{W}_{\rm tot}({\rm CO})$ for the charge-ordered ground state.

(0-0) bond, and a bond that connects a charge-rich site and a charge-poor site is denoted by a 1-0 bond. The charge patterns of the diagonal bonds in the horizontal and diagonal charge-ordered states are listed in Table I. Since there are two nonequivalent bonds for each diagonal bond in the unit cell in each charge-ordered state, we list two charge patterns in the Table. Because the charge patterns of the vertical bonds are all 1-0 pairs for these charge-ordered states, we do not list them.

The bond order for the 1-1 bond ($p(1-1)$) is the largest, that for the 0-0 bond ($p(0-0)$) is the smallest, and $2p(1-0) > p(1-1)$ holds, where $p(1-0)$ is the bond order for the 1-0 bond,

TABLE I: Charge patterns of diagonal bonds in the horizontal and diagonal charge-ordered states

Type	b1	b2	b3	b4
H1	1-0, 0-0	1-1, 1-0	1-1, 1-0	1-0, 0-0
H2	1-1, 1-0	1-0, 0-0	1-0, 0-0	1-1, 1-0
D1	1-0, 1-0	1-1, 0-0	1-0, 1-0	1-1, 0-0
D2	1-1, 0-0	1-0, 1-0	1-1, 0-0	1-0, 1-0

in the dominant b2 and b1 bonds. This is because two holes contribute to the 1-1 bond, but the virtual excitation energy in forming a 1-0 bond ($2V_{\rm V} - V_{\rm D}$) is smaller than that for a 1-1 bond ($U - V_{\rm D}$). As a result, the inequalities $G_{\rm b2}({\rm H1}) > G_{\rm b2}({\rm D2}) > G_{\rm b2}({\rm D1}) > G_{\rm b2}({\rm H2})$ and $G_{\rm b1}({\rm H2}) > G_{\rm b1}({\rm D1}) > G_{\rm b1}({\rm D2}) > G_{\rm b1}({\rm H1})$ hold, where $G_{\rm b2}({\rm H1})$ is the energy gain from the b2 bond formation in the H1-type charge-ordered state; those of other charge-order types and those for the b1 bond are denoted in the same way.

We show the θ dependence of $\bar{\beta}_{\rm Y}(0)$ in Fig. 10(c). For $10^\circ \lesssim \theta \lesssim 70^\circ$ ($-70^\circ \lesssim \theta \lesssim -30^\circ$), $|\bar{\beta}_{\rm b2}(0)|$ ($|\bar{\beta}_{\rm b1}(0)|$) is significantly larger than $|\bar{\beta}_{\rm Y}(0)|$ for the other bonds, and the energy gain from the b2 (b1) bond formation dominates the energetical order between various charge-ordered states. As a result, $W_{\rm H1}^{(\max)}$ ($W_{\rm H2}^{(\max)}$) is the largest in the region. Furthermore, $|\bar{\beta}_{\rm b2}(0)| \gg |\bar{\beta}_{\rm b1}(0)|$ holds, and $W_{\rm H1}^{(\max)}$ is much larger than those for other charge-ordered states around $\theta = 60^\circ$. The specific charge-ordered state of H1-type can be photo-generated in the region.

For $-20^\circ \lesssim \theta \lesssim -10^\circ$, $|\bar{\beta}_{\rm b1}(0)|$ is the largest but $|\bar{\beta}_{\rm b2}(0)|$ and $|\beta_{\rm b3}^{(0)}|$ are comparable to $|\bar{\beta}_{\rm b1}(0)|$. As a result of the contribution from the energy gain from b2 and b3 bond formation, the energy of the D1-type charge-ordered state drops below that of the H2-type charge-ordered state, and $W_{\rm D1}^{(\max)}$ is the largest in the region. Around $\theta = 0^\circ$, $W_{\rm tot}^{(\max)}$ becomes largest. This is because both $|\bar{\beta}_{\rm b2}(0)|$ and $|\bar{\beta}_{\rm b1}(0)|$ are significantly smaller than $|\beta_{\rm b1}^{(0)}|$ and $|\beta_{\rm b1}^{(0)}|$.

There exists an equivalent charge-ordered state to each of the horizontal charge-ordered states shown in Fig. 2(a)–(d), where all the charge-rich A or A$'$ sites and the charge-poor A or A$'$ sites are exchanged. In the θ region, where the H1-type (H2-type) charge-ordered states have dominant weights, the B (C) site is charge-rich, and the C (B) site is charge-poor; the charge density at the A site is close to 0.5 because these two equivalent states

have equal weight. The characteristic charge distribution for $10^\circ \lesssim \theta \lesssim 70^\circ$ and that for $-70^\circ \lesssim \theta \lesssim -30^\circ$, can be explained from this. There exists an equivalent charge-ordered state to each of the diagonal charge-ordered states shown in Fig. 2(e) and (f), where all the charge-rich sites and charge-poor sites are exchanged. Therefore, the charge density is nearly uniform when the diagonal charge-ordered states have dominant weight. The nearly uniform charge distribution for $-20^\circ \lesssim \theta \lesssim -10^\circ$ can be attributed to that of the D1-type charge-ordered state. The characteristic θ dependence of $\rho_{\rm X}^{(\max)}$ presented in Fig. 10(b) can be explained as changes in the dominant charge-ordered state with θ.

We have investigated the $eaA^{(\max)}$ dependence of the dynamics for $\theta = 90$, 30, 0, and -30°. Except for when $\theta = 90^\circ$, $W_{\rm tot}^{(\max)}$ increases rapidly with increasing $eaA^{(\max)}$ for $1.5 \lesssim eaA^{(\max)} \lesssim 2.5$, and $W_{\rm tot}^{(\max)}$ becomes much larger than that of charge-ordered ground state. For $\theta = 0^\circ$, $W_{\rm tot}^{(\max)}$ becomes a maximum around $eaA^{(\max)} = 2.5$, and decreases with increasing $eaA^{(\max)}$ for $eaA^{(\max)} \geq 2.5$. For $\theta = 30$ and -30°, $W_{\rm tot}^{(\max)}$ increases slowly with increasing $eaA^{(\max)}$ for $eaA^{(\max)} \geq 2.5$ and becomes a maximum around $eaA^{(\max)} = 4$.

We have succeeded to photo-generate the D1-type charge-ordered state also. We present in Fig. 11(d) the time variation of $W_{\rm Z}(t)$ for $eaA^{(\max)} = 3.87$ and $\theta = -26.7^\circ$. The D1-type charge-ordered state has dominant weight, showing that this specific charge-ordered state can be photo-generated in this instance. Around $t = -50$, where $eaA^{(\max)}(t)$ increases to about 2.3, both the H2-type and the D1-type charge-ordered states have dominant weight, which is consistent with the results of $eaA^{(\max)} = 2.3$ shown in Fig. 10(b). The averaged transfer integrals increase with increasing t for $t \geq -50$, and $\bar{\beta}_{\rm b1}(t)$ approach zero, $\bar{\beta}_{\rm b2}(t)$ become positive, and $|\bar{\beta}_{\rm b2}(t)| \gg |\bar{\beta}_{\rm b1}(t)|$ holds around $t = 0$. As a result, the H2-type charge-ordered state is strongly destabilized and the D1-type charge-ordered state becomes dominant around $t = 0$.

The remarkable increase in $W_{\rm tot}$ is not observed when $eaA^{(\max)}$ is increased to around 2.3 for $D = 10$. For $D = 60$, the peak of $W_{\rm tot}(t)$ is delayed from the pulse peak by about $0 \sim 20$, showing that the time scale for charge-order generation is comparable or slightly larger than 60. The light pulse decays before charge order is generated for $D = 10$.

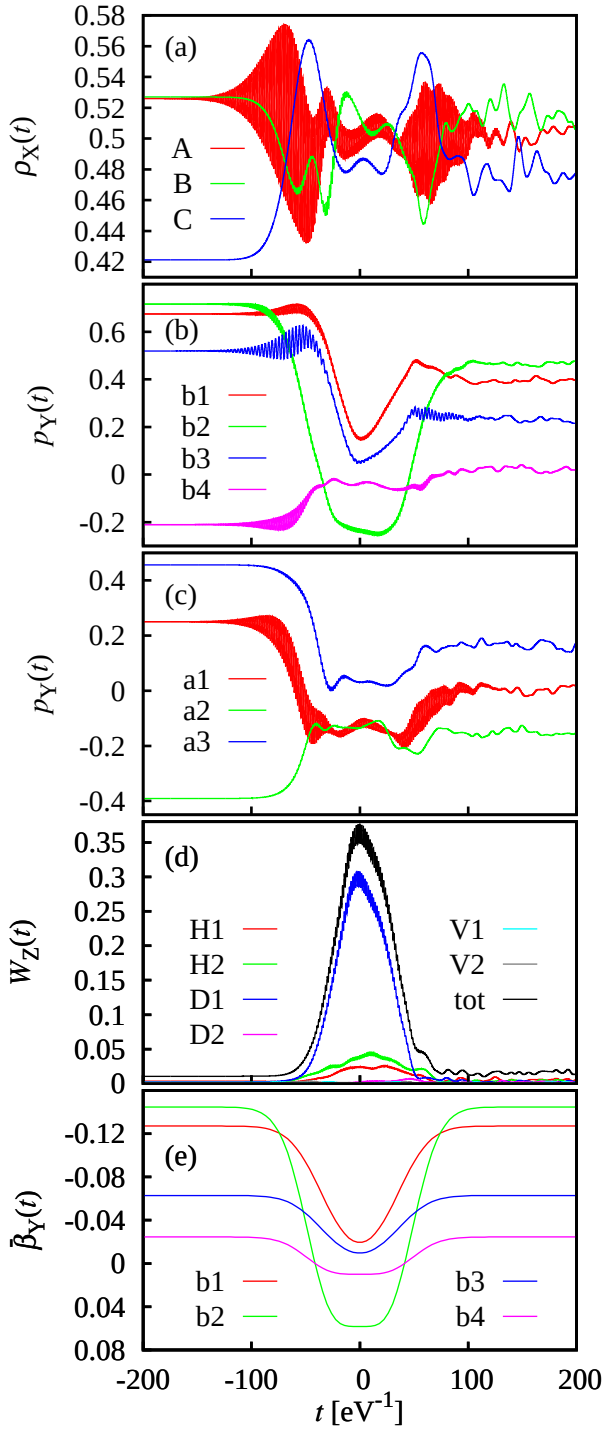

FIG. 11: (Color online) Time variation of (a) $\rho_{\rm X}(t)$, (b) $p_{\rm Y}(t)$ for diagonal bonds, (c) $p_{\rm Y}(t)$ for vertical bonds, (d) $W_{\rm Z}(t)$, and (e) $\bar{\beta}_{\rm Y}(t)$ for $eaA^{(\rm max)} = 3.87$, $\theta = -26.7^\circ$ and $D = 60$.

IV. DISCUSSION

We discuss the implications of the present results for the experimentally observed photoinduced dynamics. The peak magnitude of the electric field of the light pulse $E^{(\max)}$ used in the experiment is about 10 MV/cm. From the relation $E^{(\max)} = \omega A^{(\max)}$ and using the lattice spacing $a = 5$Å and the center frequency used in the experiment ($\omega = 0.9$), the light pulse used in experiments corresponds to $eaA^{(\max)} = 0.625$. The excitation intensity range $eaA^{(\max)} \gtrsim 2.3$, where dynamical localization occurs, corresponds to the range $E^{(\max)} \gtrsim 37$ MV/cm. As mentioned in the previous section, photoinduced changes in $\rho_{\rm X}(t)$, $p_{\rm Y}(t)$ and $W_{\rm Z}(t)$ increase slowly with increasing $eaA^{(\max)}$ around $eaA^{(\max)} = 1$, and qualitatively the same results are obtained regarding the photoinduced dynamics in the range. Therefore, we compare the results for $eaA^{(\max)} = 1$ and $D = 10$ with the experimentally observed photoinduced dynamics.

We show the results when the center frequency $\omega = 2$ is used in this paper, and this value is much larger than that used in the experiment ($\omega = 0.9$). As mentioned before, $\rho_{\rm X}(t)$, $p_{\rm Y}(t)$ and $W_{\rm Z}(t)$ are nearly independent of ω except for the rapidly oscillating components for $\omega \gtrsim 2$. This shows that a center frequency is far-off resonance for $\omega \gtrsim 2$. Despite the light absorption spectrum $\alpha(\omega)$ being very small around $\omega = 0.9$ with the present parameter set, the dynamics significantly depends on ω, showing that a real excitation to high-energy excited states is not negligible around $\omega = 0.9$.

To investigate the weak resonance effect, we here compare the results for $\omega = 2$ and those for $\omega = 0.9$. The following results hold irrespective of polarization directions θ. The main features in the time profiles of $\rho_{\rm X}(t)$, $p_{\rm Y}(t)$ and $W_{\rm Z}(t)$ for $\omega = 2$ remain for $\omega = 0.9$. This shows that the photoinduced dynamics is mainly driven by the photoinduced changes in the ratio $|\bar{\beta}_{\rm b2}(t)|/|\bar{\beta}_{\rm b1}(t)|$ also in the weak resonance case with the photon energy used in the experiment. However, there are minor differences between these two cases. During excitation by the light pulse, the rapidly oscillating component of $\rho_{\rm A}(t)$ for $\omega = 0.9$, is much larger than that for $\omega = 2$. In the time interval after the pump pulse has decayed, the time averages of $\rho_{\rm X}(t)$ for $\omega = 0.9$ are closer to 0.5 than those for $\omega = 2$; also, the time averages of $p_{\rm Y}(t)$ for $\omega = 0.9$ are closer to 0 than those for $\omega = 2$. These results also show that real excitations, which weaken the charge disproportionation and bonds, are more significant for $\omega = 0.9$. Furthermore, the amplitudes of photoinduced oscillations in $\rho_{\rm B}(t)$, $\rho_{\rm C}(t)$, and

$W_{\rm tot}(t)$ for $\omega = 0.9$, are smaller than those for $\omega = 2$. It is difficult to determine from the present result whether the reduction is attributable to the real excitation or another weak resonance effect. Dynamical localization does not occur even around $eaA^{(\max)} = 2.3$ for $\omega = 0.9$. A real excitation to high-energy excited states is significant under intense excitation, and such excitations destroy the charge order and hinder dynamical localization.

In the experimental work reported by Kawakami *et al.*[17,18], it is believed that an increase in the transient reflectivity $\Delta R/R$ for $\omega > 0.6$ eV shows a local charge-order generation, and $\Delta R/R$ shows the magnitude of the photo-generated charge order. $\Delta R/R > 0$ has been shown to survive for about 40 fs after photoexcitation, and $\Delta R/R$ oscillates with a period of 20 fs.

In our theoretical results, a periodical increase in the weight of charge-ordered states $W_{\rm tot}(t)$ is observed after the pump pulse has gone off. The increase results mainly from photoinduced three collective modes, and the period of the highest energy mode (31 fs) roughly agrees with that of $\Delta R/R$. Therefore, this experimental observation can be attributed to the collective motion of precursory phenomena for dynamical localization. The mode does not decay in our numerical calculations. This is because the decay mechanism such as the interaction with the heat bath is not included in the present model.

We have not considered the lattice motion in the present work despite the charge-ordered states being stabilized through lattice deformation. However, because lattice deformations require time scales of intermolecular vibrations, which are estimated to be about 100 fs, the effect of deformation is not important in the time interval considered here.

$\Delta R/R$ at the delay time of 30 fs after the excitation has been shown experimentally to be largest around $\theta = 0^\circ$. The conclusion from this observation is that a short-range charge order is induced efficiently from the metallic phase for the pump polarization $\theta \simeq 0^\circ$. The dynamics after the excitation of a weakly resonant single-cycle pulse has been theoretically analyzed in Ref. 18. It has been shown that the reduction of the time-averaged density-density correlation for the a2 or a3 bond, which indicates 1010 charge order generation along these bonds, is the largest at $\theta = 0 \sim 10^\circ$, and this result is consistent with the experimentally observed dynamical localization related phenomena cooperated with the Coulomb interaction and the characteristic lattice structure. As shown in the previous section, $W_{\rm tot}(t)$ exhibits a complicated oscillation after the pump pulse has gone off. The peak values in the time interval also strongly depend on θ, and their θ dependence is roughly the same as that

of $W_{\rm tot}^{(\max)}$. Specifically, for $eaA^{(\max)} = 1$, the peak values of $W_{\rm tot}(t)$ in the time interval are the largest around $\theta = 50°$.

To address the discrepancy, we investigated the dynamics with various pulse parameters. We fixed the maximum amplitude to its realistic value $eaA^{(\max)} = 1$, and considered photon energies $\omega = 0.9$ and 2, and duration times $D = 5$, 10, and 60. A single-cycle pulse used in the theoretical part of Ref. 18 can be roughly reproduced for $\omega = 0.9$ and $D = 5$. The characteristic θ dependence of the time-averaged density-density correlation for the a2 or a3 bond obtained in Ref. 18 can be reproduced only under weak resonance excitation case by nearly a single-cycle pulse ($\omega = 0.9$ and $D = 5$). The characteristic θ dependence is not observed in the weak resonance case ($\omega = 0.9$) with the duration time $D = 10$ close to that used in the experiment and also for far-off resonance ($\omega = 2$) with $D = 5$. In contrast, the main features in the time profiles of $\rho_{\rm X}(t)$, $p_{\rm Y}(t)$ and $W_{\rm Z}(t)$ remain regardless of ω and D.

For $eaA^{(\max)} = 2.3$, where dynamical localization occurs, the peak values are largest and charge order is induced most efficiently around $\theta = 0°$. This is because effective transfer integrals are strongly reduced for all the b bonds in this instance.

V. CONCLUSION

We investigated charge localization induced by higher-frequency off-resonance light-pulse excitation in the metallic phase of α-(BEDT-TTF)$_2$I$_3$. Around $eaA^{(\max)} = 1$, the charge distribution is significantly changed by photoexcitation, and the light-pulse-induced collective charge oscillations continue after photoexcitation. Furthermore, the charge dynamics depend strongly on the polarization direction of the pump pulse. These results are consistent with experiment. The magnitudes of the effective transfer integrals are reduced by strong photoexcitation, and this precursory phenomenon for dynamical localization is mainly driven by a photoinduced change in the ratio of the effective transfer integrals between the two strongest b1 and b2 bonds. For $eaA^{(\max)} \gtrsim 2$, the photoinduced transition to a charge-ordered state occurs because of dynamical localization, and the photo-generated charge-ordered state can be regarded as a light-dressed state. The type of photo-generated charge-ordered state can be controlled by choosing $eaA^{(\max)}$ and the polarization direction.

VI. ACKNOWLEDGMENTS

This work was supported by JSPS KAKENHI Grant Number JP16K05402. We thank Richard Haase, Ph.D, from Edanz Group (www.edanzediting.com/ac) for editing a draft of this manuscript.

---

* Corresponding author: takahashi.akira@nitech.ac.jp

[1] Y. Tokura, J. Phys. Soc. Jpn. **75**, 011001 (2006).

[2] K. Yonemitsu and K. Nasu, J. Phys. Soc. Jpn. **75**, 011008 (2006).

[3] K. Yonemitsu and K. Nasu, Phys. Rep. **465**, 1 (2008).

[4] K. Nasu, Eur. Phys. J. B **75**, 415 (2010).

[5] D. N. Basov, R. D. Averitt, D. van der Marel, M. Dressel, and K. Haule, Rev. Mod. Phys. **83**, 471 (2011).

[6] H. Matsuzaki, M. Iwata, T. Miyamoto, T. Terashige, K. Iwano, S. Takaishi, M. Takamura, S. Kumagai, M. Yamashita, R. Takahashi, Y. Wakabayashi, and H. Okamoto, Phys. Rev. Lett. **113**, 096403 (2014).

[7] L. Rettig, R. Cortés, J.-H. Chu, I. R. Fisher, F. Schmitt, R. G. Moore, Z.-X. Shen, P. S. Kirchmann, M. Wolf, and U. Bovensiepen, Nat. Commun. **7**, 10459 (2016).

[8] A. Singer, S. K. K. Patel, R. Kukreja, V. Uhlir, J. Wingert, S. Festersen, D. Zhu, J. M. Glownia, H. T. Lemke, S. Nelson, M. Kozina, K. Rossnagel, M. Bauer, B. M. Murphy, O. M. Magnussen, E. E. Fullerton, and O. G. Shpyrko, Phys. Rev. Lett. **117**, 056401 (2016).

[9] K.W. Kim, A. Pashkin, H. Schäfer, M. Beyer, M. Porer, T.Wolf, C. Bernhard, J. Demsar, R. Huber, and A. Leitenstorfer, Nature Mater. **11**, 497 (2012).

[10] A. Takahashi, H. Gomi, and M. Aihara, Phys. Rev. B **66**, 115103 (2002).

[11] D. Fausti, R. I. Tobey, N. Dean, S. Kaiser, A. Dienst, M. C. Hoffmann, S. Pyon, T. Takayama, H. Takagi, and A. Cavalleri, Science **331**, 189 (2011).

[12] D. Nicoletti and A. Cavalleri, Adv. Opt. Photonics **8**, 401 (2016).

[13] K. Itoh, H. Itoh, M. Naka, S. Saito, I. Hosako, N. Yoneyama, S. Ishihara, T. Sasaki, and S. Iwai, Phys. Rev. Lett. **110**, 106401 (2013).

[14] K. Onda, S. Ogihara, K. Yonemitsu, N. Maeshima, T. Ishikawa, Y. Okimoto, X. Shao, Y.

Nakano, H. Yamochi, G. Saito, and S. Y. Koshihara, Phys. Rev. Lett. **101**, 067403 (2008).

[15] L. Guérin, J. Hébert, M. Buron-LeCointe, S. I. Adachi, S. Y. Koshihara, H. Cailleau, and E. Collet, Phys. Rev. Lett. **105**, 246101 (2010).

[16] M. Servol, N. Moisan, E. Collet, H. Cailleau, W. Kaszub, L. Toupet, D. Boschetto, T. Ishikawa, A. Moréac, S. Koshihara, M. Maesato, M. Uruichi, X. Shao, Y. Nakano, H. Yamochi, G. Saito, and M. Lorenc, Phys. Rev. B **92**, 024304 (2015).

[17] T. Ishikawa, Y. Sagae, Y. Naitoh, Y. Kawakami, H. Itoh, K. Yamamoto, K. Yakushi, H. Kishida, T. Sasaki, S. Ishihara, Y. Tanaka, K. Yonemitsu, and S. Iwai, Nat. Commun. **5**, 5528 (2014).

[18] Y. Kawakami, Y. Yoneyama, T. Amano, H. Itoh, K. Yamamoto, Y. Nakamura, H. Kishida, T. Sasaki, S. Ishihara, Y. Tanaka, K. Yonemitsu, and S. Iwai, Phys. Rev. B **95**, 201105(R) (2017).

[19] H. Seo, C. Hotta, and H. Fukuyama, Chem. Rev. **104**, 5005 (2004).

[20] H. Seo, J. Merino, H. Yoshioka, and M. Ogata, J. Phys. Soc. Jpn. **75**, 051009 (2006).

[21] T. Takahashi, Y. Nogami, and K. Yakushi, J. Phys. Soc. Jpn. **75**, 051008 (2006).

[22] K. Miyagawa, A. Kawamoto, and K. Kanoda, Phys. Rev. B **62**, R7679 (2000).

[23] R. Chiba, H. Yamamoto, K. Hiraki, T. Takahashi, and T. Nakamura, J. Phys. Chem. Solids **62**, 389 (2001).

[24] M. Watanabe, Y. Noda, Y. Nogami, and H. Mori, J. Phys. Soc. Jpn. **73**, 116 (2004).

[25] Y. Takano, K. Hiraki, H. M. Yamamoto, T. Nakamura, and T. Takahashi, J. Phys. Chem. Solids **62**, 393 (2001).

[26] Y. Takano, K. Hiraki, H. M. Yamamoto, T. Nakamura, and T. Takahashi, Synth. Met. **120**, 1081 (2001).

[27] T. Kakiuchi, Y. Wakabayashi, H. Sawa, T. Takahashi, and T. Nakamura, J. Phys. Soc. Jpn. **76**, 113702 (2007).

[28] K. Yamamoto, S. Iwai, S. Boyko, A. Kashiwazaki, F. Hiramatsu, C. Okabe, N. Nishi, and K. Yakushi, J. Phys. Soc. Jpn. **77**, 074709 (2008).

[29] P. Lunkenheimer, B. Hartmann, M. Lang, J. Müller, D. Schweitzer, S. Krohns, and A. Loidl, Phys. Rev. B **91**, 245132 (2015)

[30] Y. Yue, K. Yamamoto, M. Uruichi, C. Nakano, K. Yakushi, S. Yamada, T. Hiejima, and A. Kawamoto, Phys. Rev. B **82**, 075134 (2010).

[31] F. Nad, P. Monceau, and H. M. Yamamoto, Phys. Rev. B **76**, 205101 (2007).

[32] S. Iwai, K. Yamamoto, A. Kashiwazaki, F. Hiramatsu, H. Nakaya, Y. Kawakami, K. Yakushi,

H. Okamoto, H. Mori, and Y. Nishio, Phys. Rev. Lett. **98**, 097402 (2007).

[33] S. Iwai, K. Yamamoto, F. Hiramatsu, H. Nakaya, Y. Kawakami, and K. Yakushi, Phys. Rev. B **77**, 125131 (2008).

[34] H. Nakaya, K. Itoh, Y. Takahashi, H. Itoh, S. Iwai, S. Saito, K. Yamamoto, and K. Yakushi, Phys. Rev. B **81**, 155111 (2010).

[35] Y. Kawakami, T. Fukatsu, Y. Sakurai, H. Unno, H. Itoh, S. Iwai, T. Sasaki, K. Yamamoto, K. Yakushi, and K. Yonemitsu, Phys. Rev. Lett. **105**, 246402 (2010).

[36] M. Chollet, L. Guérin, N. Uchida, S. Fukaya, H. Shimada, T. Ishikawa, K. Matsuda, T. Hasegawa, A. Ohta, H. Yamochi, G. Saito, R. Tazaki, S. Adachi, and S. Koshihara, Science **307**, 86 (2005).

[37] S. Miyashita, Y. Tanaka, S. Iwai, and K. Yonemitsu, J. Phys. Soc. Jpn. **79**, 034708 (2010).

[38] H. Gomi, A. Takahashi, T. Tastumi, S. Kobayashi, K. Miyamoto, J. Lee, and M. Aihara, J. Phys. Soc. Jpn. **80**, 034709 (2011).

[39] H. Hashimoto, H. Matsueda, H. Seo, and S. Ishihara, J. Phys. Soc. Jpn. **83**, 123703 (2014).

[40] H. Hashimoto, H. Matsueda, H. Seo, and S. Ishihara, J. Phys. Soc. Jpn. **84**, 113702 (2015).

[41] H. Hashimoto and S. Ishihara, Phys. Rev. B **96**, 035154 (2017)

[42] D. H. Dunlap and V. M. Kenkre, Phys. Rev. B **34**, 3625 (1986).

[43] F. Grossmann, T. Dittrich, P. Jung, and P. Hänggi, Phys. Rev. Lett. **67**, 516 (1991).

[44] Y. Kayanuma, Phys. Rev. A **50**, 843 (1994).

[45] Y. Naitoh, Y. Kawakami, T. Ishikawa, Y. Sagae, H. Itoh, K. Yamamoto, T. Sasaki, M. Dressel, S. Ishihara, Y. Tanaka, K. Yonemitsu, and S. Iwai, Phys. Rev. B **93**, 165126 (2016).

[46] N. Tsuji, T. Oka, P. Werner, and H. Aoki, Phys. Rev. Lett. **106**, 236401 (2011).

[47] N. Tsuji, T. Oka, H. Aoki, and P. Werner, Phys. Rev. B **85**, 155124 (2012).

[48] K. Yonemitsu and K. Nishioka, J. Phys. Soc. Jpn. **84**, 054702 (2015).

[49] H. Yanagiya, Y. Tanaka, and K. Yonemitsu, J. Phys. Soc. Jpn. **84**, 094705 (2015).

[50] A. Ono, H. Hashimoto, and S. Ishihara, Phys. Rev. B **94**, 115152 (2016).

[51] A. Ono, H. Hashimoto, and S. Ishihara, Phys. Rev. B **95**, 085123 (2017).

[52] We adopt the transfer integrals for the charge-ordered phase deduced from the extended Hückel calculation:$\beta^{(0)}_{\mathrm{a1}} = 0.0308$, $\beta^{(0)}_{\mathrm{a1'}} = 0.0495$, $\beta^{(0)}_{\mathrm{a2}} = 0.0544$, $\beta^{(0)}_{\mathrm{a3}} = -0.0329$, $\beta^{(0)}_{\mathrm{b1}} = -0.1212$, $\beta^{(0)}_{\mathrm{b1'}} = -0.1652$, $\beta^{(0)}_{\mathrm{b2}} = -0.1577$, $\beta^{(0)}_{\mathrm{b2'}} = -0.1773$, $\beta^{(0)}_{\mathrm{b3}} = -0.0673$, $\beta^{(0)}_{\mathrm{b3'}} = -0.0656$, $\beta^{(0)}_{\mathrm{b4}} = -0.0039$, and $\beta^{(0)}_{\mathrm{b4'}} = -0.0323$,[27] and the following Coulomb parameters: U =0.9, V_{V} =0.44, and V_{D} =0.40.

The calculated charge densities for the charge-ordered ground state (the experimentally obtained charge densities in the charge-ordered phase[27]) are: $\bar{\rho}_{\rm A}$ =0.81 (0.82), $\bar{\rho}_{\rm A'}$ =0.28 (0.29), $\bar{\rho}_{\rm B}$ =0.70 (0.68), and $\bar{\rho}_{\rm C}$ =0.22 (0.23).

[53] K. Yonemitsu, J. Phys. Soc. Jpn. **86**, 024711 (2017).

[54] K. Yonemitsu, J. Phys. Soc. Jpn. **86**, 064702 (2017).

[55] Y. Tanaka and K. Yonemitsu, J. Phys. Soc. Jpn. **77**, 034708 (2008).

[56] S. Miyashita and K. Yonemitsu, J. Phys. Soc. Jpn. **77**, 094712 (2008).